Polarized Autler–Townes splitting of Rydberg six-wave mixing

2016 J. Phys. B: At. Mol. Opt. Phys. 49 174002

(http://iopscience.iop.org/0953-4075/49/17/174002)

IOP Publishing Journal of Physics B: Atomic, Molecular and Optical Physics
J. Phys. B: At. Mol. Opt. Phys. **49** (2016) 174002 (7pp) doi:10.1088/0953-4075/49/17/174002

Polarized Autler–Townes splitting of Rydberg six-wave mixing

Junling Che[1,2], Yiqi Zhang[2], Yufei Zhang[2], Jun Liu[2], Qiyuan Cheng[2] and Yanpeng Zhang[2]

[1] School of Science, Xi'an University of Posts and Telecommunications, Xi'an 710121, People's Republic of China
[2] Key Laboratory for Physical Electronics, Devices of the Ministry of Education & Shaanxi Key Lab of Information Photonic Technique, Xi'an Jiaotong University, Xi'an 710049, People's Republic of China

E-mail: ypzhang@mail.xjtu.edu.cn

Received 12 January 2016, revised 14 June 2016
Accepted for publication 24 June 2016
Published 15 August 2016

Abstract

Polarized Autler–Townes (AT) splitting of six-wave mixing (SWM) involving Rydberg atoms is for the first time observed in a thermal vapor cell. By scanning the frequency detuning of the dressing field, AT splitting of Rydberg SWM is compared with that of non-Rydberg SWM with an elliptically polarized probe field. It is demonstrated that the AT spectra are strongly dependent on the interaction between Rydberg atoms. Moreover, AT splitting of SWM is cyclically modulated via a multi-dark state and presented by the corresponding spatial SWM AT splitting images. The theoretical calculations are in good agreement with the experimental results.

Keywords: Rydberg, six-wave mixing, Autler–Townes splitting

(Some figures may appear in colour only in the online journal)

1. Introduction

Since the development of laser spectroscopy in the middle of last century, nonlinear optical phenomena have attracted lots of attention. For example, the Autler–Townes (AT) splitting was first observed in the microwave domain [1] and electromagnetically induced transparency (EIT) was demonstrated by Harris *et al* [2]. As typical quantum interference effects, they are used to directly measure the Rabi frequency [3], depasing rate of Rydberg states [4] and so on. Rydberg atoms, which have a large principal quantum number, possess many intriguing properties [5–7], one of which is the excitation blockade effect [8, 9] due to the strong interaction between Rydberg atoms, which makes Rydberg atoms a candidate for quantum gates and information processes [10–12]. AT splitting of Rydberg atoms has been intensely investigated in the magneto-optical trap (MOT). But as far as we know, AT splitting of Rydberg in thermal vapors has not been reported before. Due to the scalability and simplicity, Rydberg atoms in thermal environments are more applicable in quantum information processes. Also, EIT, a useful tool for the investigation of thermal Rydberg [13–15], has attracted lots of attention. Thus, we extend Rydberg to higher order nonlinear processes in thermal vapors [16] with AT splitting. This research will be an important step toward quantum information storage schemes [17].

In this paper, we report theoretical and experimental results about the polarized AT splitting of Rydberg (SWM) in a five-level atomic system of ^{85}Rb as well as the characteristics of AT splitting for non-Rydberg which are cyclically modulated by multi-dark state. Firstly, we observe the polarized AT splitting of Rydberg and non-Rydberg SWM processes via changing probe field detuning. Secondly, AT splitting of two SWM processes will be studied with a different power of optical field. Finally, non-Rydberg SWM is cyclically modulated by polarization of the dressing field and spatial AT splitting is presented.

2. Experimental setup

The experiment is performed in an atomic vapor cell. The 5 cm long rubidium cell is wrapped by μ-metal and heated via heater tape to 65 °C. The energy levels $5S_{1/2}(F = 2)$, $5S_{1/2}(F = 3)$, $5P_{3/2}(F = 3)$, $45D_{5/2}$ and $5D_{5/2}(F = 2)$ constitute a five-level system as shown in figure 1(a). The probe laser beam $\mathbf{E}_1$

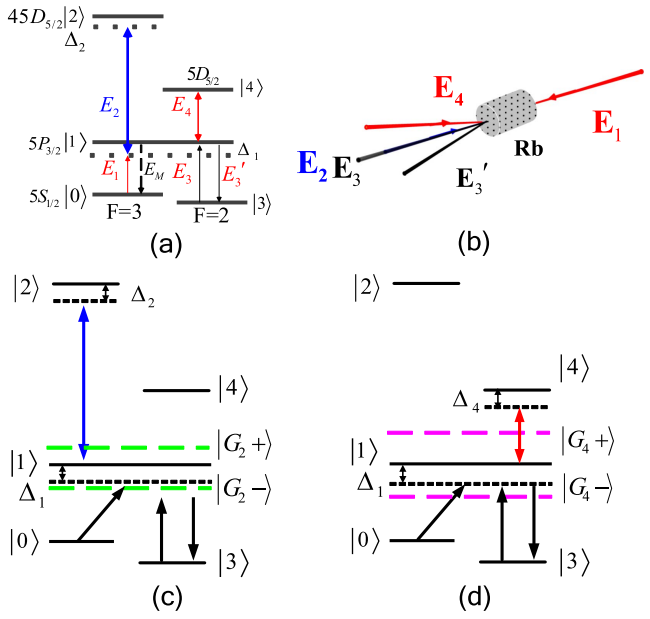

Figure 1. (a) Schematic of atomic system to produce multi-wave mixing (MWM) signals. (b) Optical paths of our experiment. (c), (d) Dressed energy levels by $\mathbf{E}_2$ and $\mathbf{E}_4$, respectively.

(wavelength of 780.244 nm resonates with the transition of $5S_{1/2}(F = 3)$ ($|0\rangle$) to $5P_{3/2}(F = 3)$ ($|1\rangle$)) is horizontally polarized provided by an external cavity diode laser (ECDL). The laser beam $\mathbf{E}_2$, driving $5P_{3/2}(F = 3)$ ($|1\rangle$) to $45D_{5/2}$ ($|2\rangle$) with the vertical polarization is from the second commercial laser consisting of an ECDL and a frequency doubling to 480 nm with a linewidth <2 MHz. The beams $\mathbf{E}_3$ and $\mathbf{E}'_3$ (wavelength of 780.235 nm, connects the transition $5P_{3/2}(F = 3)$ ($|1\rangle$) and $5S_{1/2}(F = 2)$ ($|3\rangle$)) are split from the third ECDL with the horizontal polarization. The laser beam $\mathbf{E}_4$ (wavelength of 776.157 nm, connects transition $5P_{3/2}(F = 3)$ ($|1\rangle$) to $5D_{5/2}(F = 2)$ ($|4\rangle$)) is from the fourth ECDL with the horizontal polarization. The propagation directions and geometric distributions of all these beams are presented in figure 1(b). The diameters of the beam $\mathbf{E}_1$, $\mathbf{E}_2$, $\mathbf{E}_3$, and $\mathbf{E}_4$ are about 0.8, 1, 1 and 0.9 mm, respectively.

In such a five-level atomic system, two coupled laser fields ($\mathbf{E}_2$ and $\mathbf{E}_4$) separately generate the two ladder-type EIT windows with free Doppler configuration. One is related to the Rydberg state $45D_{5/2}$, and the other is related to non-Rydberg state $5D_{5/2}$. Energy levels $|3\rangle$ and $|1\rangle$ are coupled by two pump fields $\mathbf{E}_3$ and $\mathbf{E}'_3$, together with $|0\rangle$ form the three-level Λ-type subsystem, which makes a four-wave mixing (FWM) without EIT window satisfying the phase matching condition $\mathbf{k}_{\mathrm{FWM}} = \mathbf{k}_3 + \mathbf{k}_3 - \mathbf{k}'_3$, where $\mathbf{k}_i$ is the wave vector of corresponding optics field. The generated FWM is diffracted from the opposite direction of $\mathbf{E}'_3$ and is detected by an avalanche photodiode. The probe transmission signal is detected simultaneously by the other avalanche photodiode. Combining with this classical FWM, $\mathbf{E}_2$ and $\mathbf{E}_4$ as the dressing fields can generate two SWM processes. First, without $\mathbf{E}_4$, a Rydberg SWM process is generated via the perturbation chain

$$\rho_{00}^{(0)} \xrightarrow{\omega_1} \rho_{10}^{(1)} \xrightarrow{-\omega_3} \rho_{30}^{(2)} \xrightarrow{\omega_3} \rho_{10}^{(3)} \xrightarrow{\omega_2} \rho_{20}^{(4)} \xrightarrow{-\omega_2} \rho_{10}^{(5)}$$

satisfying the phase match condition $\mathbf{k}_{S1} = \mathbf{k}_1 + \mathbf{k}_3 - \mathbf{k}'_3 + \mathbf{k}_2 - \mathbf{k}_2$. The field $\mathbf{E}_2$ dresses level $|1\rangle$ and creates the primarily-dressed states $|+\rangle$ and $|-\rangle$ as shown in figure 1(c). Similarly, for SWM of $5D_{5/2}$ generated by $\mathbf{E}_4$ without $\mathbf{E}_2$, it utilizes the perturbation chain

$$\rho_{00}^{(0)} \xrightarrow{\omega_1} \rho_{10}^{(1)} \xrightarrow{-\omega_3} \rho_{30}^{(2)} \xrightarrow{\omega_3} \rho_{10}^{(3)} \xrightarrow{\omega_4} \rho_{20}^{(4)} \xrightarrow{-\omega_4} \rho_{10}^{(5)}$$

satisfying $\mathbf{k}_{S2} = \mathbf{k}_1 + \mathbf{k}_3 - \mathbf{k}'_3 + \mathbf{k}_4 - \mathbf{k}_4$. $\mathbf{E}_4$ can also dress level $|1\rangle$ to create the primarily-dressed states $|+\rangle$ and $|-\rangle$ as shown in figure 1(d).

In general, the two primarily-dressed states induced by $\mathbf{E}_2$ can be written as $|\pm\rangle = \sin\theta_{1\pm}|1\rangle + \cos\theta_{1\pm}|2\rangle$. The density matrix element $\rho_{10}^{(5)(1)}$ can be obtained via solving the coupled density matrix equations [18], as

$$\rho_{10}^{(5)(1)} = \frac{i\,|G_1|^{0.2}(|G_2|/n^{11})^{0.4}|G_3|^2}{[d_1 + |G_1|^2/\Gamma_{00} + (|G_2|/n^{11})^{0.4}/d_2]^3 d_2 d_3}. \quad (1)$$

where $d_1 = \Gamma_{10} + i\Delta_1$, $d_2 = \Gamma_{20} + i(\Delta_1 + \Delta_2)$, $d_3 = \Gamma_{30} + i(\Delta_1 - \Delta_3)$, Γ_{ij} is the transverse relaxation rate between $|i\rangle \leftrightarrow |j\rangle$, G_i is the Rabi-frequency corresponding to optical field $\mathbf{E}_i$, and $\Delta_i = \omega_i - \omega_{ij}$ is the detuning of optical field $\mathbf{E}_i$ (ω_i is the laser frequency of $\mathbf{E}_i$, ω_{ij} is the resonant transition frequency between $|i\rangle \leftrightarrow |j\rangle$). Considering Rydberg strong interaction, we modify $G_2 \xrightarrow{\text{interaction}} (G_2/n^{11})^{0.2}$ via the mean field model [19]. Similarly, primarily-dressed states induced by $\mathbf{E}_4$ can be written as $|\pm\rangle = \sin\theta_{1\pm}|1\rangle + \cos\theta_{1\pm}|4\rangle$, so

$$\rho_{10}^{(5)(2)} = \frac{i\,|G_1|\,|G_3|^2\,|G_4|^2}{[d_1 + |G_1|^2/\Gamma_{00} + |G_4|^2/d_4]^3 d_3 d_4}. \quad (2)$$

where $d_4 = \Gamma_{40} + i(\Delta_1 + \Delta_4)$.

A stronger probe field $\mathbf{E}_1$ can participate in the generation of SWM fields and dress the involved energy level which in turn affects the SWM process. At first, $\mathbf{E}_2$ dresses $|1\rangle$ and creates the primary dressed states $|\pm\rangle$ at a proper frequency detuning (tuned to be close to $|+\rangle$ or $|-\rangle$). This process generates AT splitting of the SWM signal. The eigenvalues of two primary dressed states induced by $\mathbf{E}_2$ are $\lambda_\pm = (\Delta_2 \pm \sqrt{\Delta_2 + 4\,|G_2^{0.2}|^2}\,)/2$. If $\mathbf{E}_1$ is weak ($G_1 \ll G_2$), the primary AT separation Δa is mainly determined by $\mathbf{E}_2$, i.e., $\Delta a = \lambda_+ - \lambda_- \approx 2G_2^{0.2}$, while, if $\mathbf{E}_1$ is strong enough, Δa is determined by both $\mathbf{E}_2$ and $\mathbf{E}_1$. When $\mathbf{E}_4$ comes into play, the eigenvalues of primarily-dressed state are $\lambda_\pm{}' = (\Delta_4 \pm \sqrt{\Delta_4 + 4\,|G_4|^2}\,)/2$ and $\Delta a' = \lambda_+{}' - \lambda_-{}' \approx 2G_4$.

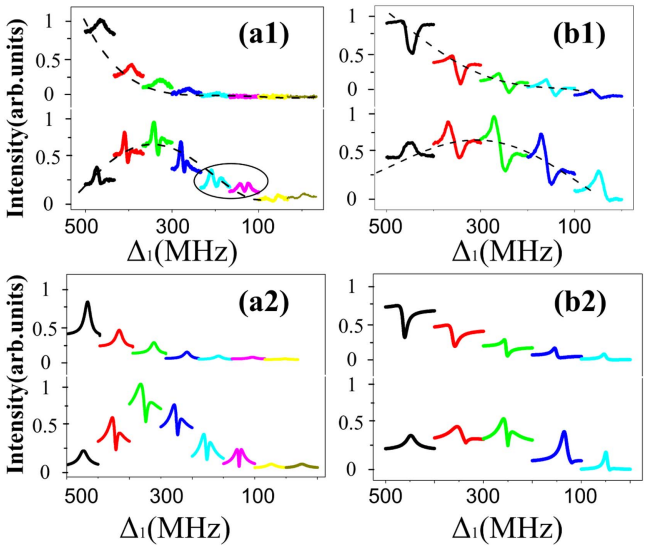

Figure 2. (a1) Measured Rydberg probe transmission and SWM signals for different detuning of $\mathbf{E}_1$. (b1) Same as (a1) but for the non-Rydberg case. (a2), (b2) Simulation results corresponding to (a1) and (b1).

3. Results and discussions

Firstly, we set the probe field to be elliptically polarized, probe transmission and SWM signals at different probe field detuning Δ_1.

Figure 2(a1) shows the probe transmission and SWM signals of 45D with different Δ_1. For probe transmission, each peak as EIT satisfies two photons resonance condition $\Delta_1 + \Delta_2 = 0$. With Δ_1 changing from 500 MHz to 0, the EIT peak becomes small. Surprisingly, the smallest EIT peak is generated, because weak $\mathbf{E}_1$ and $\mathbf{E}_3$ pumping effect suppresses the atom absorption. In this process, the Rydberg SWM AT splitting in thermal vapor is firstly observed. Such AT splitting is in the condition of the elliptically polarized probe field, so we call it polarized AT splitting. It is clear from figure 2(a1) that the Rydberg SWM changes from a single peak to AT splitting and to a weak peak at last with Δ_1 changes from 500 MHz to 0. The dashed line (i.e. the baseline of SWM) is the FWM generated by $\mathbf{E}_1$, $\mathbf{E}_3$ and $\mathbf{E}'_3$. When FWM is the strongest at $\Delta_1 = 350$ MHz, the Rydberg SWM AT splitting dip is the deepest, whereas it becomes weak if Δ_1 decreases to 100 MHz and also the two peaks are same at $\Delta_1 = 120$ MHz. To explain this phenomenon, we utilize equation (1) to simulate the experimental results as shown in figure 2(a2), which agrees with our experimental results. Due to the Rydberg interaction, the dressing effect in equation (1) is modified as $(|G_2|/n^{11})^{0.4}/d_2$. The dressing effect of $\mathbf{E}_2$ becomes weak gradually with increasing principal quantum number n. For higher Rydberg states, the weaker dressing effect makes SWM splitting hard to detect unless the polarized dressing beam participates. Figure 2(b) presents the non-Rydberg $5D_{5/2}$ cases in the same condition. One can see from figure 2(b1) that the probe transmission changes from all suppression dip (EIA) to half suppression and half enhancement then to weak peak (EIT) with Δ_1 changing from 500 MHz to 0. As mentioned

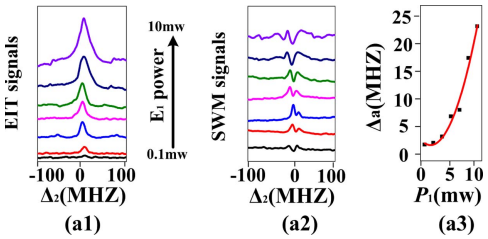

Figure 3. Measured Rydberg probe transmission (a1) and SWM signals (a2) versus Δ_2 for $\Delta_1 = 300$ MHz under different P_1. (a3) AT splitting separation of the Rydberg SWM signals with increasing of P_1.

above, the EIT peak which is caused by $\mathbf{E}_4$ and satisfies $\Delta_1 + \Delta_4 = 0$ emerges in a certain range of the probe detuning. While the EIA dip that satisfies $\Delta_1 + \Delta_4 = |G_4|^2/\Delta_1$ will appear at a large probe detuning such as $\Delta_1 = 500$ MHz. Different Δ_1 determines different shape of probe transmission. A similar case can be observed for Rydberg; the peak which ought to the strongest becomes the weakest due to $\mathbf{E}_1$ and $\mathbf{E}_3$. As to SWM in figure 2(b1), the SWM signals change from a peak to AT splitting till to half peak and half dip. Comparing with Rydberg, because non-Rydberg has a bigger dipole moment, its SWM presents half suppression and half enhancement. In addition, one cannot see the AT splitting of the two peaks, and the reason is that elliptically polarized probe field enhances the dressing effect, which suppresses the peak of non-Rydberg SWM. Figure 2(b2) is the corresponding simulation results according to equation (2), which is in accordance with (b1).

In the following, the Rydberg probe transmission and SWM variation of different power of $\mathbf{E}_1$ (P_1), $\mathbf{E}_2$ (P_2) and $\mathbf{E}_3$ (P_3) with $\Delta_1 = 300$ MHz are investigated. Figure 3 shows that the Rydberg probe transmission signals (a1) and SWM (a2) increase with power of $\mathbf{E}_1$ by scanning dressing field. The single peak is the EIT window but the SWM is AT splitting generated by $\mathbf{E}_2$ and becomes strong with increased P_1. In each SWM signal of figure 3(a2), the splitting peaks increase first and then decrease, while the middle dip is always getting stronger. As a result, SWM with AT splitting is inverted when P_1 increases to 10 mw. Figure 3(a3) is the corresponding dependence curve of the AT splitting separation that varies with the increasing of P_1, one can find that the AT splitting separation remains unchanged at first and gets larger with increasing of P_1. The reason that such regularity appears is when the probe field $\mathbf{E}_1$ is weak, the AT splitting separation mainly depends on $\mathbf{E}_2$ field. But when $\mathbf{E}_1$ is strong enough, the AT splitting separation is determined by both $\mathbf{E}_2$ and $\mathbf{E}_1$.

If only P_2 increases as shown in figure 4 with $P_1 = 100$ μw fixed, one can see that the EIT peak becomes bigger and bigger, but for SWM the left peak is lower than the right peak at the beginning and then becomes higher. These results resemble another group's research in ultracold Rydberg atoms [20], which can demonstrate the profiles of AT splitting are influenced by Rydberg atoms interaction. The corresponding dependence curve is presented in figure 4(a3), which shows that the separation of AT splitting grows with increasing of power P_2 according to $\Delta_a = \lambda_+ - \lambda_- = 2G_2^{0.2}$.

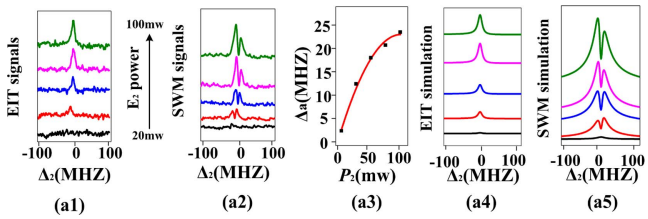

Figure 4. Measured Rydberg probe transmission (a1) and SWM signals (a2) versus Δ_2 for $\Delta_1 = 300$ MHz under different P_2. (a3) AT splitting separation of the Rydberg SWM signals with increasing of P_2. Simulation results of the Rydberg probe transmission (a4) and the SWM signals (a5) corresponding to (a1) and (a2), respectively.

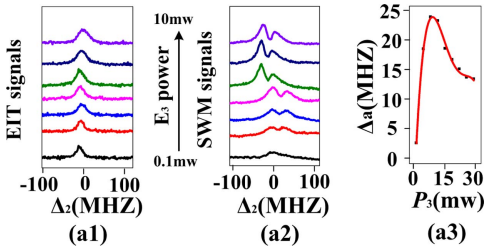

Figure 5. Measured Rydberg probe transmission (a1) and SWM signals (a2) versus Δ_2 for $\Delta_1 = 300$ MHz under different P_3. (a3) AT splitting separation of the Rydberg SWM signals dependence with P_3.

If only the power of $\mathbf{E}_3$ increases, the height of EIT peak remains almost unchanged but its line width becomes wider due to the pumping effect of the $\mathbf{E}_3$ field. For SWM the two peaks and the middle dip become high and deep at first, respectively, and then remain invariant. But the AT splitting separation increases to the maximum quickly and then decreases, which can be seen in figure 5(a3). In order to explain this variation, we appeal to the density-matrix element

$$\begin{aligned}\rho_{10}^{(5)} &= i|G_1|^{0.2}(|G_2|/n^{11})^{0.4}|G_3|^2/\{d_1 + |G_1|^2/\Gamma_{00} \\ &+ (|G_2|/n^{11})^{0.4}/d_2 - |G_3|^2/[i(\Delta_1 - \Delta_3) + \Gamma_{30}]\}^3 \\ &\times d_2 d_3 = G_a\{1-3(|G_2|/n^{11})^{0.4}/d_1 d_2 \\ &+ 12(|G_2|/n^{11})^{0.4}|G_3|^2/d_1{}^2 d_2\,[i(\Delta_1 - \Delta_3) \\ &+ \Gamma_{30}]...\},\end{aligned} \tag{3}$$

where $G_a = i\,|G_1|^{0.2}(|G_2|/n^{11})^{0.4}|G_3|^2/d_1^3 d_2 d_3$. The first term in equation (3) represents a five-photon process and the second term seven-photon process that can destroy the first term, so that the AT splitting is generated. But the third term, a nine-photon process, possesses the same character with the first term, which leads to SWM signals to be increased. Thus, the separation of AT splitting decreases with P_3 increases to certain degree, then the third term begins to be dominant.

As a comparison, we also present the non-Rydberg SWM signals versus Δ_4 with different power in figure 6, which is quite different from the Rydberg SWM. Here, with Δ_4 scanned, AT splitting is primarily caused by the dressing effect of $\mathbf{E}_4$. The left peak of splitting is

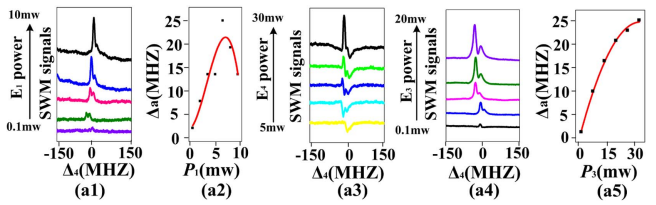

Figure 6. Measured non-Rydberg SWM signals versus Δ_4 for $\Delta_1 = 300$ MHz under P_1 (a1), P_4 (a3) and P_3 (a4), respectively. (a2) AT splitting separation of the non-Rydberg SWM signals dependence with P_1. (a5) Same as (a2) but with P_3.

$\lambda'_- = (\Delta_4 - \sqrt{\Delta_4 + 4|G_4|^2})/2$ and the right is $\lambda'_+ = (\Delta_4 + \sqrt{\Delta_4 + 4|G_4|^2})/2$. The separation of SWM is mainly determined by P_4, but with P_1 increasing, $\mathbf{E}_1$ begins to play and the splitting distance becomes large. When P_1 goes up to a certain degree, the strongest dressing effect of $\mathbf{E}_1$ and big dipole moment can make the separation of SWM become small as shown in figures 6(a1) and (a2).

Due to the elliptically polarized probe field, a SWM suppressing dip appears when $\mathbf{E}_4$ is weak. With P_4 increasing, the switch of suppressing dip and enhancement peak can be observed in figure 6(a3) so that AT splitting is destroyed. Figure 3(a4) shows the changes in SWM with P_3, which is the same with Rydberg. However, it does not have a seven-photon process, the splitting separation just increases with increasing P_3. The dependence of splitting separation on P_3 is presented in figure 6(a5), where the solid curve indicate the theoretical result, which is in accordance with the experimental results (dots).

Last but not least, by changing the polarization of the dressing field with a half-wave plate (HWP) or quarter-wave plate (QWP), AT splitting of non-Rydberg SWM can be modulated. The experimental results are shown in figures 7 and 8, with Δ_1 being scanned with different polarization of the dressing field. Figures 7(a) and (b) show the change of the SWM spectrum by rotating the HWP. When $\mathbf{E}_2$ is blocked, only the non-Rydberg SWM signal is left. We analyze the height variation between the left peak and the dip, the right peak and the dip, as well as the left peak and the right peak in order to quantitatively observe AT splitting variation of SWM signals more clear with different dressing field polarizations. As shown in figure 7(b), in which the black curve in figure 7(b1) represents height variation between the left peak and the dip, the red curve shows the variation between the right peak and the dip. The distances between the left peak and the right peak at different dressing field polarization are shown in figure 7(b2).

When the polarization directions of linearly polarized $\mathbf{E}_4$ are changed via HWP, only 15 nonzero components are independent on the basis of the relation for Rb vapor of isotropic medium

$$\begin{aligned}\chi_{xxxxxx} &= \chi_{yyxxxx} + \chi_{yxyxxx} + \chi_{yxxyxx} + \chi_{yxxxyx} + \chi_{yxxxxy} \\ &+ \chi_{xyyxxx} + \chi_{xyxyxx} + \chi_{xyxxyx} + \chi_{xyxxxy} + \chi_{xxyyxx} \\ &+ \chi_{xxyxyx} + \chi_{xxyxxy} + \chi_{xxxyxy} + \chi_{xxxyyx} + \chi_{xxxxyy}.\end{aligned} \tag{4}$$

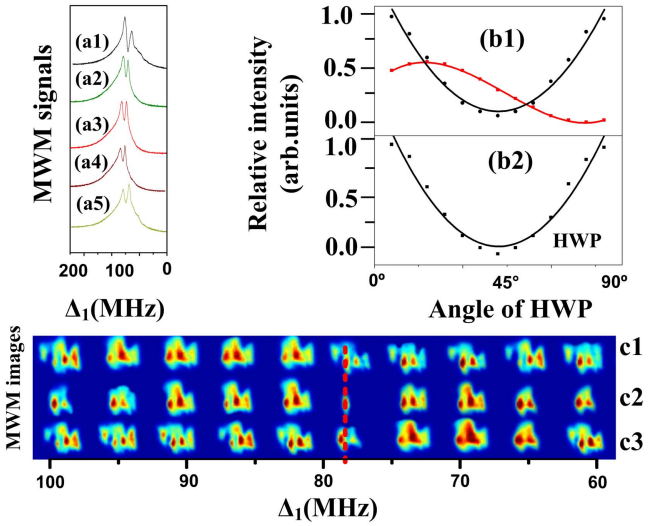

Figure 7. (a) Measured SWM spectrum versus Δ_1 with different polarization of $\mathbf{E}_4$ by rotating the HWP. (b) The change rules of the SWM spectrum in (a). (c) Measured images of MWM signals when θ of HWP is 0° (c1), 45° (c2), 90° (c3).

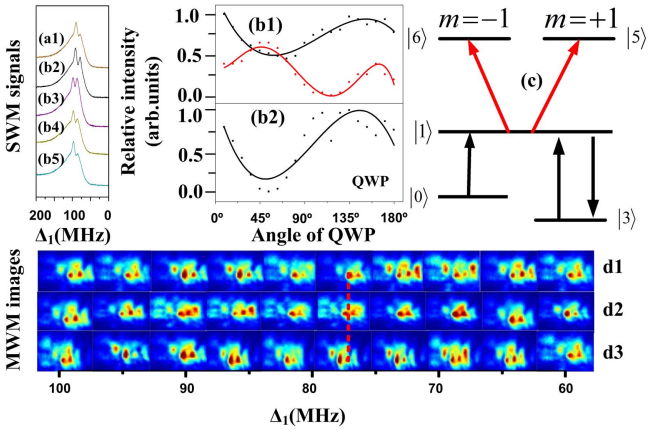

Figure 8. (a) Measured SWM spectrum versus Δ_1 with different polarization of $\mathbf{E}_4$ by rotating the QWP. (b) The change rules of the SWM spectrum in (a). (c) Sub-energy level of circularly polarized $\mathbf{E}_4$ field. (d) Measured images of MWM signals when θ of QWP is 0° (d1), 45° (d2), 90° (d3).

The polarization of the generated SWM has two components, which are parallel and perpendicular to the polarization

$$\begin{aligned}\chi_x &= \chi_{xyyyxy}\cos 2\theta \\ \chi_y &= \chi_{yyyyyy}\sin 2\theta.\end{aligned} \tag{5}$$

Therefore, $\rho_{10}^{(5)(2)}$ determining intensity of non-Rydberg SWM can be modified as

$$\rho_{10_x}^{(5)(2)} = \sum \frac{iG_1|G_3|^2|c_xG_4\cos(2\theta)|^2}{\left(\Gamma_{10}+i\Delta_1+\dfrac{|c_xG_4\cos(2\theta)|^2}{\Gamma_{40}+i(\Delta_1+\Delta_4)}\right)^3(\Gamma_{30}+i(\Delta_1-\Delta_3))(\Gamma_{40}+i(\Delta_1+\Delta_4))}, \tag{6}$$

$$\rho_{10_y}^{(5)(2)} = \sum \frac{iG_1\,|G_3|^2\,|c_yG_4\sin(2\theta)|^2}{\left(\Gamma_{10}+i\Delta_1+\dfrac{|c_yG_4\sin(2\theta)|^2}{\Gamma_{40}+i(\Delta_1+\Delta_4)}\right)^3(\Gamma_{30}+i(\Delta_1-\Delta_3))(\Gamma_{40}+i(\Delta_1+\Delta_4))}, \tag{7}$$

$$\rho_{10_{x-y}}^{(5)(2)} = \sum_M \frac{iG_1\,|G_3|^2|G_4(c_y\sin(2\theta)+c_x\cos(2\theta))|^2}{\left(\Gamma_{10}+i\Delta_1+\dfrac{|G_4(c_y\sin(2\theta)+c_x\cos(2\theta))|^2}{\Gamma_{40}+i(\Delta_1+\Delta_4)}\right)^3(\Gamma_{30}+i(\Delta_1-\Delta_3))(\Gamma_{40}+i(\Delta_1+\Delta_4))}, \tag{8}$$

where $c_{x,y}$ is the anisotropic factor denoting the different susceptibilities χ_{xyyyxy} and χ_{yyyyyy} in different polarization directions. θ is the angle of HWP.

In figure 7(b), it is interesting to see the polarization dependence of the SWM emission signal follows classical polarization relation of the dressing field. However, one can find that the rules of evolution in the relative height of the left peak and right peak are opposite in figure 7(b1). The different change rules of the two SWM peaks can be attributed to the modulation of the polarized dressing field. The different anisotropic factors c_x, c_y in equations (6)–(8), denoting different susceptibilities χ_{xyyyxy}, χ_{yyyyyy} in different directions, have different dressing effects for the SWM process. These factors result in the rule of evolution variation in the relative height of the left peak and the right peak. As far as the distance variation between the right peak and left peak in figure 7(b2) is concerned, its regularity is the same as the variation of the left peak and dip because the left peak variation degree is always larger than that of the right peak.

In addition, the images of non-Rydberg MWM in figure 7(c) show that the spatial AT splitting changes with different dressing field polarization directions. In figure 7(c1), we can find that the third image from the left reflects the left peak of the SWM AT splitting while the eighth image

represents the right peak corresponding to figure 7(a1). Images in figure 7(c1) are those intensities of the left peak of AT splitting which are stronger than that of the right peak; in figure 7(c2), we can find that the intensity of the left peak is similarly equal to the right peak which corresponds to the SWM spectrum shown in figure 7(a3). Figure 7(c3) is corresponding to figure 7(a5). In these spatial images, the spatial splitting can be observed, which reflects the phase shift caused by the dressing field.

The splitting of SWM images can be explained by the nonlinear phase shift $\phi = 2k_{p,F}zn_2^{XE_4}I_4e^{-(\zeta-\zeta_4)^2/2}/(n_0I_{p,F})$ and spatial alignment of $\mathbf{E}_1$ and $\mathbf{E}_4$. In detail, the propagation wave equation depicts self- and cross- phase modulation induced spatial interplay of MWM is

$$\frac{\partial u_M}{\partial Z} - \frac{\partial^2 u_M}{2\partial\zeta^2} = \frac{ik_M^2 w_0^2 I}{n_0}(n_2^{SM}\ |u_M|^2 + 2n_2^{X1}\ |u_4|^2)u_M \tag{9}$$

where n_2^{SM} is the self-Kerr nonlinear coefficient of MWM, n_2^{X1} is the cross-Kerr nonlinear coefficient of $\mathbf{E}_4$. The Kerr nonlinear coefficient determines defocusing (focusing) effect when the sign is negative (positive). For the nonlinear phase shift, ζ_4 is the center of $\mathbf{E}_4$. Therefore, the additional transverse propagation wave-vectors introduced by $\mathbf{E}_i$ are $\delta k_{i\zeta} = (\partial\phi_i/\partial\zeta)\hat{\zeta}$, $\delta k'_{i\zeta} = (\partial\phi'_i/\partial\zeta)\hat{\zeta}$, and $\delta k''_{i\zeta} = (\partial\phi''_i/\partial\zeta)\hat{\zeta}$ where $\hat{\zeta}$ is the unit vector. The direction of $\delta k_{i\zeta}$ determines the spatial characteristics of MWM in the transverse dimension. For $\Delta_1 > 0$, the atomic system is defocusing due to self-Kerr nonlinearly $n_2^{SM} < 0$. In this case, $\delta k_{i\zeta}$ always points to the beam center of the weak field, so the weak fields shift away from the strong field. Moreover, MWM partly overlaps with $\mathbf{E}_4$ mainly in the horizontal (x) direction and splits in the direction because SWM is repulsed by $\mathbf{E}_4$ with refractive index variation $\Delta n^{XE_4} < 0$ caused by the cross-Kerr effect. When Δ_1 reaches to the resonant point, Δn^{XE_4} becomes large enough so that MWM shifts along the x-direction. Besides, according to the phase shift ϕ, if the intensity of SWM is stronger, ϕ will be smaller, so we can see two splitting optical spots generated by $\partial\phi'_i/\partial x$. Such a splitting is lower than the right part in figure 7(c1). Three splitting spots appear due to the weaker dressing effect of $\mathbf{E}_4$, which means that ϕ is bigger, which can be well explained by $\partial\phi''_i/\partial x^2$.

The SWM intensity spectra modulated by QWP are shown in figure 8(a) and the corresponding dependence curves are shown in figure 8(b). One can find that the evolution in the relative height of the left peak and dip is opposite to the right peak and dip in figure 8(b1). Although this phenomenon is also caused by dark states, there is an essential difference in physical mechanism. With QWP varying, the polarized property of optical field is changed, so the Zeeman sublevel has to be considered in the dipole transition process. Different Zeeman levels determine different transition pathways so that dark states change. When $\theta = 45°$, the beam $\mathbf{E}_4$ is right-hand circularly polarized, the corresponding Rabi frequency considering Zeeman sublevels can be represented as $G_4{}^+$. During $0° \sim 45°$ and $45° \sim 90°$, $G_4{}^+ > G_4{}^0$ (0 denotes Rabi frequency corresponding to linear polarization of $\mathbf{E}_4$), and during $90° \sim 180°$, $G_4{}^- > G_4{}^0$. The dark states are related to $G_4^{\pm}$, so $G_4^{\pm}$ can influence the change rules of the left peak and right peak of the SWM AT splitting. The different relation between $G_4^{\pm}$ and $G_4{}^0$ can vary with changing of QWP, which will result in the rule of evolution in the relative height of the left peak and the right peak as shown in figure 8(b1).

To explain the relation between the experimental results and Rabi frequency clearly, a K5e-type configuration is adopted as shown in figure 8(c). The two states $|5\rangle$ and $|6\rangle$ are degenerate Zeeman sublevels corresponding to the magnetic quantum numbers $m_F = +1$ and $m_F = -1$ respectively. The Hamiltonian of the K5e-type five-level system can be written as

$$\begin{aligned} \mathrm{H} = &-\hbar(\Delta_4\ |5\rangle\langle 5| - \Delta_3\ |3\rangle\langle 3| + \Delta_4\ |6\rangle\langle 6| \\ &- \Delta_1\ |0\rangle\langle 0|) - \hbar(G_1\ |0\rangle\langle 1| + G_4{}^+\ |5\rangle\langle 1| \\ &+ G_3\ |3\rangle\langle 1| + G_4{}^-\ |6\rangle\langle 1| + \mathrm{h.\,c.}). \end{aligned} \tag{10}$$

Under the resonant conditions $\Delta_1 + \Delta_4 = 0$, $\Delta_2 = 0$ and $\Delta_3 = 0$, we can easily get four identified dark states

$$|D'1\rangle = \frac{G_4{}^-\ |0\rangle - G_1\ |5\rangle}{\sqrt{|G_1|^2 + |G_4{}^-|^2}} \approx |0\rangle - \frac{G_1}{G_4{}^-}\ |5\rangle \tag{11a}$$

$$|D'2\rangle = \frac{G_3\ |0\rangle - G_1\ |3\rangle}{\sqrt{|G_3|^2 + |G_1|^2}} \approx |0\rangle - \frac{G_1}{G_3}\ |3\rangle \tag{11b}$$

$$|D'3\rangle = \frac{G_4{}^+\ |0\rangle - G_1\ |6\rangle}{\sqrt{|G_4{}^+|^2 + |G_1|^2}} \approx |0\rangle - \frac{G_1}{G_4{}^+}\ |6\rangle \tag{11c}$$

$$|D'4\rangle = \frac{G_3\ |6\rangle - G_4{}^+\ |3\rangle}{\sqrt{|G_3|^2 + |G_4{}^+|^2}} = \cos\theta\ |6\rangle - \sin\theta\ |3\rangle. \tag{11d}$$

where $\cos\theta = G_3/\sqrt{|G_3|^2 + |G_4^+|^2}$ and $\sin\theta = G_4^+/\sqrt{|G_3|^2 + |G_4^+|^2}$. The total dark state amplitude is then given by

$$\begin{aligned} |D'\rangle &= |D'1\rangle + |D'2\rangle + |D'3\rangle + |D'4\rangle \\ &= 3\ |0\rangle - \frac{G_1}{G_4{}^-}\ |5\rangle - \left(\frac{G_1}{G_4{}^+} - \cos\theta\right)|6\rangle \\ &\quad - \left(\frac{G_1}{G_3} + \sin\theta\right)|3\rangle. \end{aligned} \tag{12}$$

We want to see how the populations of the atoms in the dark states vary as the four non coupled states interfere with each other. That is, we would like to find $|\langle D'|\psi\rangle|^2$. The wave function of the atom in its bare-state basis is written as

$$|\psi\rangle = c_0\ |0\rangle + c_1\ |1\rangle + c_2\ |3\rangle + c_3\ |5\rangle + c_4\ |6\rangle \tag{13}$$

From equations (11) and (12), we get

$$|\langle D'|\psi\rangle|^2 = 9\rho_{00} + \left(\frac{G_1}{G_4^-}\right)^2\rho_{22} + \left(\frac{G_1}{G_3} + \sin\theta\right)^2\rho_{33} + \left(\frac{G_1}{G_4^+} - \cos\theta\right)^2\rho_{44} + 2\,\mathrm{Re}\left\{-3\frac{G_1}{G_4^-}\rho_{20} - 3\left(\frac{G_1}{G_3} + \sin\theta\right)\rho_{30} - 3\left(\frac{G_1}{G_4^+} - \cos\theta\right)\rho_{40} + \frac{G_1}{G_4^-}\left(\frac{G_1}{G_3} + \sin\theta\right)\rho_{32} + \frac{G_1}{G_4^-}\left(\frac{G_1}{G_4^+} - \cos\theta\right) \times \rho_{42} + \left(\frac{G_1}{G_3} + \sin\theta\right)\left(\frac{G_1}{G_4^-} - \cos\theta\right)\rho_{43}\right\} \quad (14)$$

where $\rho_{\mathrm{nm}} = c_m c_n$ is the elements of the density-matrix operator

$$\rho_{20} = \frac{iG_4^-}{d_2}\frac{iG_1}{d_1 + |G_4^-|^2/d_2 + |G_3|^2/d_3 + |G_4^+|^2/d_4}\rho_{00} \quad (15a)$$

$$\rho_{30} = \frac{iG_3^*}{d_3}\frac{iG_1}{d_1 + |G_4^-|^2/d_2 + |G_3|^2/d_3 + |G_4^+|^2/d_4}\rho_{00} \quad (15b)$$

$$\rho_{40} = \frac{iG_4^+}{d_4}\frac{iG_1}{d_1 + |G_4^-|^2/d_2 + |G_3|^2/d_3 + |G_4^+|^2/d_4}\rho_{00} \quad (15c)$$

$$\rho_{21} = -\frac{iG_1{}^*}{d_{21} + |G_3|^2/d_8 + |G_4^-|^2/d_7'}\rho_{20} \quad (15d)$$

$$\rho_{31} = -\frac{iG_1{}^*}{d_{31} + |G_4^-|^2/d_8' + |G_4^+|^2/d_9'}\rho_{30} \quad (15e)$$

$$\rho_{41} = -\frac{iG_1{}^*}{d_{41} + |G_4^-|^2/d_7 + |G_3|^2/d_9}\rho_{40} \quad (15f)$$

$$\rho_{32} = (-iG_4^{-*}\rho_{31} + iG_3{}^*\rho_{12})/d_8' \quad (15g)$$

$$\rho_{42} = (-iG_4^{-*}\rho_{41} + iG_4^+\rho_{12})/d_7 \quad (15h)$$

$$\rho_{43} = (-iG_3\rho_{41} + iG_4^+\rho_{13})/d_9 \quad (15i)$$

where $d_{31} = -i\Delta_3 + \Gamma_{31}$, $d_8 = i(\Delta_3 + \Delta_2) + \Gamma_{23}$, $d_7{}' = -i(\Delta_4 - \Delta_2) + \Gamma_{24}$, $d_8{}' = -i(\Delta_3 + \Delta_2) + \Gamma_{32}$, $d_9 = i(\Delta_3 + \Delta_4) + \Gamma_{43}$ and $d_9{}' = -i(\Delta_3 + \Delta_4) + \Gamma_{34}$. In equation (14), the assumptions $\rho_{11} \approx 0$, $\rho_{22} \approx 0$, $\rho_{33} \approx 0$, and $\rho_{44} \approx 0$ are adopted. By considering the quantum interference among $|0\rangle$, $|3\rangle$, $|5\rangle$ and $|6\rangle$, the intensity of SWM signal is $I = |N'\mu\rho_{10}^{(5)}|^2$, where $N' = N(1 - |\langle D'|\psi\rangle|^2)$.

The spatial AT splitting changed by QWP is shown in figures 8(d1)–(d3) corresponding to figures 8(a1), (a3) and (a5), respectively, which is similar to cases changed by HWP. These results demonstrate that the phase shift of spatial AT splitting can be controlled by dressing polarization.

4. Conclusion

In summary, the Rydberg SWM AT splitting in thermal vapor is observed experimentally for the first time. The results are in agreement with the theoretical results. By comparing with non-Rydberg, the influences of frequency detuning and power to AT splitting of SWM are investigated. Moreover, we have experimentally and theoretically demonstrated that Zeeman sublevels can significantly modulate the AT splitting of SWM processes as well as corresponding spatial images; these results would lay a solid foundation for spatial Rydberg research in the future.

Acknowledgments

This work was supported by the 973 Program (2012CB921804), KSTIT of Shaanxi province (2014KCT-10), and NSFC (11474228, 61308015).

References

[1] Autler S H and Townes C H 1955 *Phys. Rev.* **100** 703
[2] Harris S E, Field J E and Imamoglu A 1991 *Phys. Rev. Lett.* **66** 2593
[3] Keaveney J, Hughes I G, Sargsyan A, Sarkisyan D and Adams C S 2012 *Phys. Rev. Lett.* **109** 233001
[4] Raitzsch U, Heidemann R, Weimer H, Butscher B, Kollmann P, Löw R, Büchler H P and Pfau T 2009 *New J. Phys.* **11** 055014
[5] Gallagher T F 1994 *Rydberg Atoms* (Cambridge: Cambridge University Press)
[6] Afrousheh K, Bohlouli-Zanjanni P, Vagale D, Mugford A, Fedorov M and Martin J D D 2004 *Phys. Rev. Lett.* **93** 233001
[7] Mudrich M, Zahzam N, Vogt T, Comparat D and Pillet P 2005 *Phys. Rev. Lett.* **95** 233002
[8] Tong D, Farooqi S M, Sannojevic J, Krishnan S, Zhang Y P, Côté R and Lukin M D 2004 *Phys. Rev. Lett.* **93** 063001
[9] Vogt T, Viteau M, Chotia A, Zhao J M, Comparat D and Pillet P 2007 *Phys. Rev. Lett.* **99** 073002
[10] Jaksch D, Cirac J I, Zoller P, Rolston S L, Côté R and Lukin M D 2000 *Phys. Rev. Lett.* **85** 2208
[11] Tyler K, Krittika G, Jau Y Y, Biedermann G W, Landahl A J and Deutsch I H 2013 *Phys. Rev.* A **87** 052314
[12] Saffman M, Walker T G and Mölmer K 2010 *Rev. Mod. Phys.* **82** 2313
[13] Mohapatra A K, Jackson T R and Adams C S 2007 *Phys. Rev. Lett.* **98** 113003
[14] Huber B, Baluktsian T, Schlagmüller M, Kölle A, Kübler H, Löw R and Pfau T 2011 *Phys. Rev. Lett.* **107** 243001
[15] Baluktsian T, Huber B, Löw R and Pfau T 2013 *Phys. Rev. Lett.* **110** 123001
[16] Zhang Y P, Khadka U, Anderson B and Xiao M 2009 *Phys. Rev. Lett.* **102** 013601
[17] Lukin M D, Fleischhauer M and Cote R 2001 *Phys. Rev. Lett.* **87** 037901
[18] Nie Z, Zheng H, Li P, Yang Y, Zhang Y and Xiao M 2008 *Phys. Rev.* A **77** 063829
[19] Zhang Z Y, Zheng H B, Tian Y L, Che J L, Wang X X, Zhu D Y, Zhang Y P and Xiao M 2015 *Sci. Rep.* **5** 10462
[20] Zhang H, Wang L M, Chen J, Bao S X, Zhang L J, Zhang J M and Jia S T 2013 *Phys. Rev.* A **87** 033835